Libralato, M, Gerasimov, R, Bedin, L, Anderson, J, Apai, D, Bellini, A, Burgasser, AJ, Griggio, M, Nardiello, D, Salaris, M, Scalco, M and Vesperini, E

 JWST imaging of the closest globular clusters: IV. Chemistry, luminosity, and mass functions of the lowest-mass members in the NIRISS parallel fields

http://researchonline.ljmu.ac.uk/id/eprint/24903/

Article

Astronomy & Astrophysics

JWST imaging of the closest globular clusters

IV. Chemistry, luminosity, and mass functions of the lowest-mass members in the NIRISS parallel fields

M. Libralato[1,2,*] , R. Gerasimov[3], L. Bedin[1] , J. Anderson[4], D. Apai[5,6], A. Bellini[4], A. J. Burgasser[7],
M. Griggio[1,4,8] , D. Nardiello[9] , M. Salaris[10], M. Scalco[1], and E. Vesperini[11]

[1] INAF – Osservatorio Astronomico di Padova, Vicolo dell'Osservatorio 5, Padova 35122, Italy
[2] AURA for the European Space Agency, Space Telescope Science Institute, 3700 San Martin Drive, Baltimore, MD 21218, USA
[3] Department of Physics and Astronomy, University of Notre Dame, Nieuwland Science Hall, Notre Dame, IN 46556, USA
[4] Space Telescope Science Institute, 3700 San Martin Drive, Baltimore, MD 21218, USA
[5] Department of Astronomy and Steward Observatory, The University of Arizona, 933 N. Cherry Avenue, Tucson, AZ 85721, USA
[6] Lunar and Planetary Laboratory, The University of Arizona, 1629 E. University Blvd., Tucson, AZ 85721, USA
[7] Department of Astronomy & Astrophysics, University of California, San Diego, La Jolla, California 92093, USA
[8] Dipartimento di Fisica e Scienze della Terra, Università di Ferrara, Via Giuseppe Saragat 1, Ferrara 44122, Italy
[9] Dipartimento di Fisica e Astronomia "Galileo Galilei", Università di Padova, Vicolo dell'Osservatorio 3, Padova 35122, Italy
[10] Astrophysics Research Institute, Liverpool John Moores University, 146 Brownlow Hill, Liverpool L3 5RF, UK
[11] Department of Astronomy, Indiana University, Swain West, 727 E. 3rd Street, Bloomington, IN 47405, USA

Received 28 June 2024 / Accepted 4 September 2024

ABSTRACT

We present observations of the two closest globular clusters, NGC 6121 and NGC 6397, taken with the NIRISS detector of JWST. The combination of our new JWST data with archival Hubble Space Telescope (HST) images allows us to compute proper motions, disentangle cluster members from field objects, and probe the main sequence (MS) of the clusters down to <0.1 $M_\odot$ as well as the brighter part of the white-dwarf sequence. We show that theoretical isochrones fall short in modeling the low-mass MS and discuss possible explanations for the observed discrepancies. Our analysis suggests that the lowest-mass members of both clusters are significantly more metal-rich and oxygen-poor than their higher-mass counterparts. It is unclear whether the difference is caused by a genuine mass-dependent chemical heterogeneity, low-temperature atmospheric processes altering the observed abundances, or systematic shortcomings in the models. We computed the present-day local luminosity and mass functions of the two clusters; our data reveal a strong flattening of the mass function indicative of a significant preferential loss of low-mass stars in agreement with previous dynamical models for these two clusters. We have made our NIRISS astro-photometric catalogs and stacked images publicly available to the community.

Key words. techniques: photometric – astrometry – proper motions – globular clusters: individual: NGC 6121 – globular clusters: individual: NGC 6397

1. Introduction

Globular clusters (GCs) have been the subject of countless investigations on a wide range of topics because they are ideal laboratories for testing models of star formation and evolution. While the most massive stars in GCs have been extensively studied in recent decades, too little is known about the least massive members along the main sequence (MS) and, in particular in the regime of brown dwarfs. Very-faint objects among very-bright stars in GCs have always posed a challenge even to the Hubble Space Telescope (HST), requiring a significant amount of telescope time to be observed, if they could be observed at all (Richer et al. 2008; Dieball et al. 2016, 2019). JWST (Gardner et al. 2023) has already shown that objects with masses <0.1 $M_\odot$ and brown dwarfs are within its reach (e.g., Nardiello et al. 2023b; Marino et al. 2024).

The scientific interest in photometric observations of the lowest-mass GC members is predominantly three-fold. First, the colors of low-mass stars and brown dwarfs are sensitive to the abundances of key elements, including oxygen, titanium, carbon and alkali metals (Marley et al. 2002; Gerasimov et al. 2022b, 2024b). The sensitivity primarily arises from the extreme pressure broadening of atomic lines and dominant molecular opacity. Photometric abundances measured near the end of the MS may be compared to the spectroscopic observations of upper-MS and post-MS members to constrain the magnitude of chemical variations with stellar mass (Dotter et al. 2015; Milone et al. 2019, 2012a, 2023; Scalco et al. 2024a; Ziliotto et al. 2023; Cadelano et al. 2023). The presence or absence of such variations has been suggested as a means to differentiate between the proposed origins of the presently unexplained chemical scatter among GC members (the so-called multiple populations; see reviews in Renzini et al. 2015; Bastian & Lardo 2018; Cassisi & Salaris 2020; Milone & Marino 2022). In addition, GCs provide a unique opportunity to study the discrepancy between primordial and observed element abundances in cool stars and brown dwarfs, driven by low-temperature phenomena

such as condensation and gravitational settling of dust, and nonequilibrium chemistry. This effect is likely responsible for the disagreement between theoretical and observed brown dwarf luminosities near the hydrogen-burning limit (Marino et al. 2024), and inconsistent abundances in star or brown-dwarf binary systems (Calamari et al. 2022).

Second, the luminosity functions (LFs) of brown dwarfs and low-mass stars just above the hydrogen-burning limit are sensitive to the age of the parent population, as the energy production by nuclear fusion in the cores of these objects is insufficient to attain energy equilibrium (Kumar 1962; Hayashi & Nakano 1963; Burgasser 2004). GCs are prime candidates for this dating technique, because their old ages ($\gtrsim$12 Gyr, Carretta et al. 2000; VandenBerg et al. 2013) and large sizes ($\gtrsim 10^5$ members, Hilker et al. 2020) ensure that the stellar-substellar transition in the LF is both prominent and well populated (Gerasimov et al. 2022a, 2024b).

Third, the low-mass regime of the present-day GC mass functions (MFs) provides an important constraint on the effects of dynamical evolution, which remain the largest source of uncertainty in the estimates of the initial MF in GCs. At present, inferred MFs of GCs are largely consistent with a universal initial MF, as evident from the strong correlation between the measured MFs, central densities and dynamical relaxation times (Paust et al. 2010; Sollima & Baumgardt 2017), the lack of clear environmental dependence among less dynamically evolved clusters (Baumgardt et al. 2023), and direct comparison to simulations (Richer et al. 2008; Webb & Leigh 2015; Baumgardt & Sollima 2017). Including the lowest-mass members in MF studies not only extends the mass baseline, but also potentially probes a distinct regime of star formation (e.g., where additional formation channels for substellar objects – such as disk or filament fragmentation – need to be considered). While no clear discontinuities in the substellar MF of star clusters have been observed so far (see review in Luhman 2012), their existence is tentatively suggested by the binary properties of brown dwarfs in the field (Burgasser et al. 2003; Thies & Kroupa 2007; Thies et al. 2015; Grieves et al. 2021).

The present paper is the fourth of a series aimed at investigating the coolest sources in the two closest GCs: NGC 6121 and NGC 6397 (Bedin et al. 2024, Paper I). The first three papers of the series focused on NGC 6397, specifically, Paper I focused on the white dwarfs (WDs), Gerasimov et al. (2024a, hereafter Paper II) on the brown dwarfs, and Scalco et al. (2024b, Paper III) on the multiple populations. Here, we analyze the faint-end of the MS using the JWST's Near Infrared Imager and Slitless Spectrograph (NIRISS) camera (Doyon et al. 2012). In Section 2, we describe the data reduction in detail, including the tweaks applied to the official JWST pipeline to improve the final astrometric and photometric products. In Section 3, we discuss how we combined HST and JWST data to compute proper motions (PMs) and present color-magnitude diagrams (CMDs) of the two clusters. We compare our photometry for the two clusters with a set of isochrones in Section 4. Finally, the LFs and MFs for NGC 6121 and NGC 6397 in our fields are presented in Sect. 5.

2. Data sets and reduction

NGC 6121 and NGC 6397 were observed with JWST as part of program GO-1979 (PI: Bedin) using the Near Infrared Camera (NIRCam, Rieke et al. 2023) in primary and NIRISS in parallel. The main science goal of the program is to reach the faintest sources of these GCs in the field of view of the primary instrument. Therefore, the choices of telescope pointing, dither pattern and the observing setup are driven by the requirements of NIRCam. Figure 1 illustrates the position of our NIRISS fields with respect to the center of each cluster. Below we described the data sets and reduction procedures.

2.1. NGC 6121 data set

NGC 6121 was observed by JWST on 2023 April 9–10 in two different fields located at about the half-light radius ($r_h \sim 4.65$ arcmin according to the GC database of Holger Baumgardt[1]) from the center of the cluster (always taken from the Baumgardt database), which we refer to as the "Northern" and "Southern" fields.

The Northern field is centered at about (RA, Dec) = (245.958201, −26.544989) deg, which is ∼3.6 arcmin from the center of the cluster. The field was observed with 12 F150W-filter images in a 2×3 dither pattern (two subdithers per position) for a total field of view of 3.0×2.7 arcmin². Exposures were taken with the NIS readout, 11 groups, and one integration, for an effective exposure time of 472.418 s for each of the 12 exposures.

The Southern field is centered at about (RA, Dec) = (245.937502, −26.596299) and is located at ∼4.8 arcmin from the center of NGC 6121. Only three exposures with small dithers were taken (field of view of 2.2×2.2 arcmin²). The observing setup consisted again in F150W images with the NISRAPID readout, 11 groups and one integration (effective exposure time of 118.104 s).

Both NIRISS fields overlap (the Northern partially and the Southern completely) with existing HST data from the GO-12911 program (PI: Bedin) acquired between 2013 January 18 and May 19. This data set contains 30×180s exposures taken with the Wide Field Camera (WFC) of the Advanced Camera for Surveys (ACS) in F606W and F814W filters.

2.2. NGC 6397 data set

The NIRISS observations of NGC 6397 are centered at about (RA, Dec) = (265.372698, −53.826364) deg (∼11.5 arcmin away from the center of the cluster, i.e., $4r_h$, assuming $r_h \sim 3$ arcmin as per the Baumgardt database). The data were taken on 2023 March 14 and comprise 12 F150W-filter images organized in a 2×3 dither pattern (with two images per dither position), covering a field of view of 2.2×2.2 arcmin². Each image was obtained with the NIS readout mode, 14 groups and one integration per exposure, for an effective exposure time of 601.259 s.

Analogously to the case of NGC 6121, this NIRISS field partially overlaps with existing HST data from GO-9480 (PI: Rhodes) taken on 2003 March 27–28. This data set is made up of five ACS/WFC images (3×700 s, 1× 558 s, 1× 400 s) in the F775W filter.

2.3. JWST data reduction

We downloaded the NIRISS level-1b, uncalibrated (_uncal) fits files from the Mikulski Archive for Space Telescopes (MAST)[2]. We processed these images using the official JWST pipeline[3] version 1.12.5 (Bushouse et al. 2023) through the stages 1 and 2

---

[1] https://people.smp.uq.edu.au/HolgerBaumgardt/globular/
[2] https://mast.stsci.edu/search/ui/
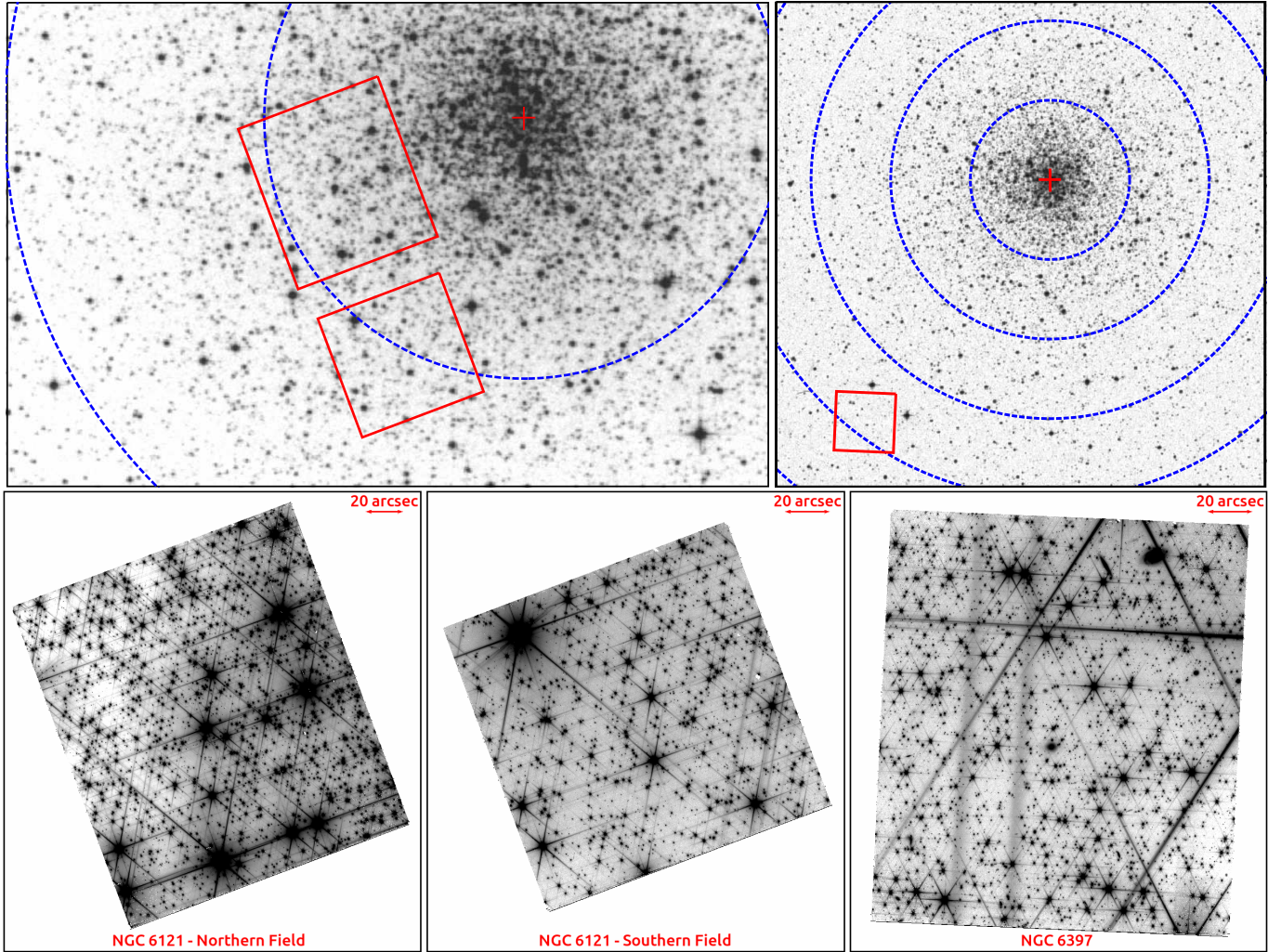[3] https://github.com/spacetelescope/jwst

Fig. 1. Analyzed field of view. Top: gray-scale infrared images of NGC 6121 (left) and NGC 6397 (right) from the Digital Sky Survey 2. The centers of the clusters (taken from the Baumgardt GC database) are highlighted with a red cross. The blue dashed circles have radii equal to N times the half-light radius, with $N = [1, 2]$ for NGC 6121 and $[1, 2, 3, 4, 5]$ for NGC 6397. The red polygons in each panel highlight the coverage of the NIRISS data. Bottom: gray-scale stacked images of NGC 6121 and NGC 6397 made with the GO-1979 NIRISS data. In all panels, north is up and east is to the left.

to obtain level-2b (`_cal`) images. We ran the pipeline using the default values for all but two steps.

First, we turned on the charge-migration step in the stage-1 pipeline and set the signal-threshold parameter of the step to 25 000. This choice allowed us to improve the photometry and astrometry for the brightest stars near saturation, which are severely affected by the brighter-fatter effect (e.g., Libralato et al. 2023; Goudfrooij et al. 2024). Second, we let the ramp-fit step to fit the ramps of saturated pixels using the first frame of each integration ("suppress_one_group" = False), which, in turn, increased the dynamical range of our data and improved measurements of saturated stars in our images. The mitigation of the brighter-fatter effect and the recovery of saturated stars were essential steps in our work because they improved the quality of the sources that are included in the *Gaia* Early Data Release 3 (EDR3) catalog (Gaia Collaboration 2016, 2021), which we used to set a common reference frame system.

We initially used the publicly available FORTRAN code `jwst1pass`[4] (Libralato et al. 2023, 2024, Anderson et al., in

preparation) to measure positions and fluxes of bright stars in each NIRISS exposure by fitting effective point-spread functions (ePSFs). The library NIRISS ePSFs were tailored for each image[5]. Positions were corrected for geometric distortion. Library ePSFs and geometric-distortion corrections were described and made publicly available for the NIRISS imager by Libralato et al. (2023).

We cross-matched bright stars in each NIRISS catalog with those in the *Gaia* EDR3 catalog. The *Gaia* catalog (projected onto a tangent plane centered at about the center of our NIRISS fields after positions were moved to the 2023 epoch by means of the *Gaia* PMs) was used to setup a common reference frame

---

[4] https://www.stsci.edu/~jayander/JWST1PASS/CODE/

[5] In each image, we found bright, unsaturated stars and measured their position and flux using the library ePSF models. We then subtracted a model of each star based on the parameters obtained from the fit. The residuals of the subtraction were collected in a grid, the size of which varies from a 1×1 to a 5×5 depending on the number of sources at disposal, and then averaged. Finally, the ePSF models were modified according to the residual grid (a linear interpolation was used to obtain the ePSF perturbation at any given location). The entire process was iterated nine times.

system. We imposed that the x and y axes point towards west and north, respectively, and fixed the pixel scale to 40 mas pixel^{-1} to somewhat better sample the image stacks. We iteratively cross-identified the same stars in all images, and applied six-parameter linear transformations[6] to transform stellar positions in each NIRISS catalog onto the master frame. The NIRISS photometry was registered to that of a NIRISS single-image catalog. Once on the same reference system, positions and instrumental magnitudes were averaged to create a preliminary astro-photometric catalog.

The final stage of the data reduction was obtained using a NIRISS-tailored version of the software KS2 (Anderson et al., in prep.; see also Bellini et al. 2017a; Libralato et al. 2022). KS2 performs the so-called second-pass photometry, which makes use of all images at once to detect objects too faint to be measured in a single image. Also, KS2 measures all sources after all close-by neighbors have been ePSF subtracted from the image. The astro-photometric catalogs made by KS2 contain several diagnostic parameters that can be used to select a sample of well-measured stars. We refer the reader to Libralato et al. (2022) for a complete description of the outputs of KS2.

KS2 does not measure saturated stars, for which positions and fluxes are taken from the output of the first-pass photometry (see discussion in Bellini et al. 2017a). Saturated and very-bright stars are used by KS2 to construct appropriate masks around them to prevent the software from detecting PSF artifacts. In our fields, there are many very bright stars for which modeling some PSF features is a complex task; also, these stars can extend for thousands of pixels (Fig. 1). For this reason, we made use of the Python package WebbPSF (Perrin et al. 2012, 2014), which can provide simulated PSFs for all JWST imagers taking into account models of the telescope and optical state of an instrument but not detector effects. A single WebbPSF PSF of 3072×3072 NIRISS pixel^2 was placed at the position and rescaled by the flux of each saturated/very bright star (which is similar fashion to what is done during the ePSF-fitting stage) to make these masks. Although not perfect, this step allowed us to reject most of the PSF artifacts around bright objects.

The photometric calibration of our NIRISS catalogs was performed as follows. First, we used the stage-3 pipeline of JWST to combine all `_cal` fits files of each field and make a level-3 (`_i2d`) mosaic image. We then measured the flux of bright and unsaturated stars in this `_i2d` image via aperture photometry using as aperture radius that enclosing the 70% of the total energy of a point source. The sky was estimated in an annulus region with inner and outer radii enclosing the 80% and 85% of the total energy, respectively. These radii are provided by the aperture-correction reference file[7] of NIRISS in the JWST Calibration Reference Data System (CRDS). We chose these values because they allow us to directly use the official NIRISS aperture corrections to correct our photometry for the finite aperture. We converted the aperture-corrected surface brightness (the unit of the `_i2d` images is MJy sr^{-1}) of each star to a flux density in Jansky using the conversion factor provided in the fits header and then defined the magnitudes in the VEGAmag system as:

$$m_{\text{VEGA}} = -2.5 \times \log(\text{flux density}) + 8.9 + \text{ZP}_{\text{VEGA}}$$
$$= m_{\text{AB}} + \text{ZP}_{\text{VEGA}},$$

---

[6] Almost all sources in the NIRISS data in common with the *Gaia* EDR3 catalog are saturated. Thus, we used saturated stars for the initial registration on the *Gaia* reference frame. Once the master frame was set up, we only used bright, unsaturated stars in the process.

[7] Reference file: "jwst_niriss_apcorr_008.fits".

where ZP$_{\text{VEGA}}$ is the AB-to-VEGA zero-point available in CRDS[8]. Finally, we cross-identified the same stars in our KS2-based and aperture-based catalogs and computed a zero-point to add to the KS2 instrumental magnitudes to put them in the calibrated VEGAmag system. These zero-points are 33.184 and 31.684 for the Northern- and Southern-field photometry of NGC 6121, respectively, and 33.447 for the photometry of NGC 6397.

2.4. HST data reduction

The HST data reduction was performed on `_flc` images (unre-sampled exposures that are dark and bias corrected, flat-fielded, and pipeline-corrected for the charge-transfer-efficiency defects as described in Anderson & Ryon 2018) through a combination of first- and second-pass photometric stages as previously described for JWST. We made use of publicly available library ePSFs and geometric-distortion corrections[9] (Anderson & King 2006). The master frame was again setup by means of the *Gaia* EDR3 catalog after positions were moved to the epoch of the HST observations.

The calibration of the KS2-based HST instrumental magnitudes was obtained using the `_drc` (for ACS/WFC or WFC3/UVIS) images, the official aperture corrections and VEGA-mag zero-points[10] (see Bellini et al. 2017a).

3. A first look at the CMDs

For each cluster and field, the astro-photometric catalogs made with HST and JWST data were combined by cross-identifying the same stars in both catalogs. Positions as measured in the HST catalog were transformed onto the reference frame of the JWST catalog by means of six-parameter linear transformations. The coefficients of these transformations were computed using only bright, unsaturated cluster stars (iteratively identified through their location on the CMD and their positional displacement). Relative PMs were defined as the positional displacements between epochs divided by the average temporal baseline and multiplied by the pixel scale of the reference frame (40 mas pixel^{-1}). Because we selected cluster stars as a reference, our PMs are computed relative to the bulk motion of cluster. This means that in the vector-point diagram (VPD), the distribution of the cluster members is centered at $(0, 0)$ by construction, and all other objects are placed in a region of the VPD according to their motion relative to the cluster. In the following, the photometry used in all CMDs has been corrected for systematic errors using artificial-star tests as described in Appendix B.

3.1. NGC 6121

The HST-JWST CMDs of NGC 6121 are shown in Fig. 2 (panels a and b). Photometry is corrected for the effects of the differential reddening as in Milone et al. (2012b) and Bellini et al. (2017b), assuming E($B - V$)=0.37 from Hendricks et al. (2012). Black markers represent unsaturated cluster members, while saturated stars are plotted in red. Open circles and dots refer to

---

[8] Reference file: "jwst_niriss_abvegaoffset_0003.asdf".

[9] https://www.stsci.edu/~jayander/HST1PASS/

[10] See the resources provided here: https://www.stsci.edu/hst/instrumentation/acs/data-analysis https://www.stsci.edu/hst/instrumentation/wfc3/data-analysis/photometric-calibration
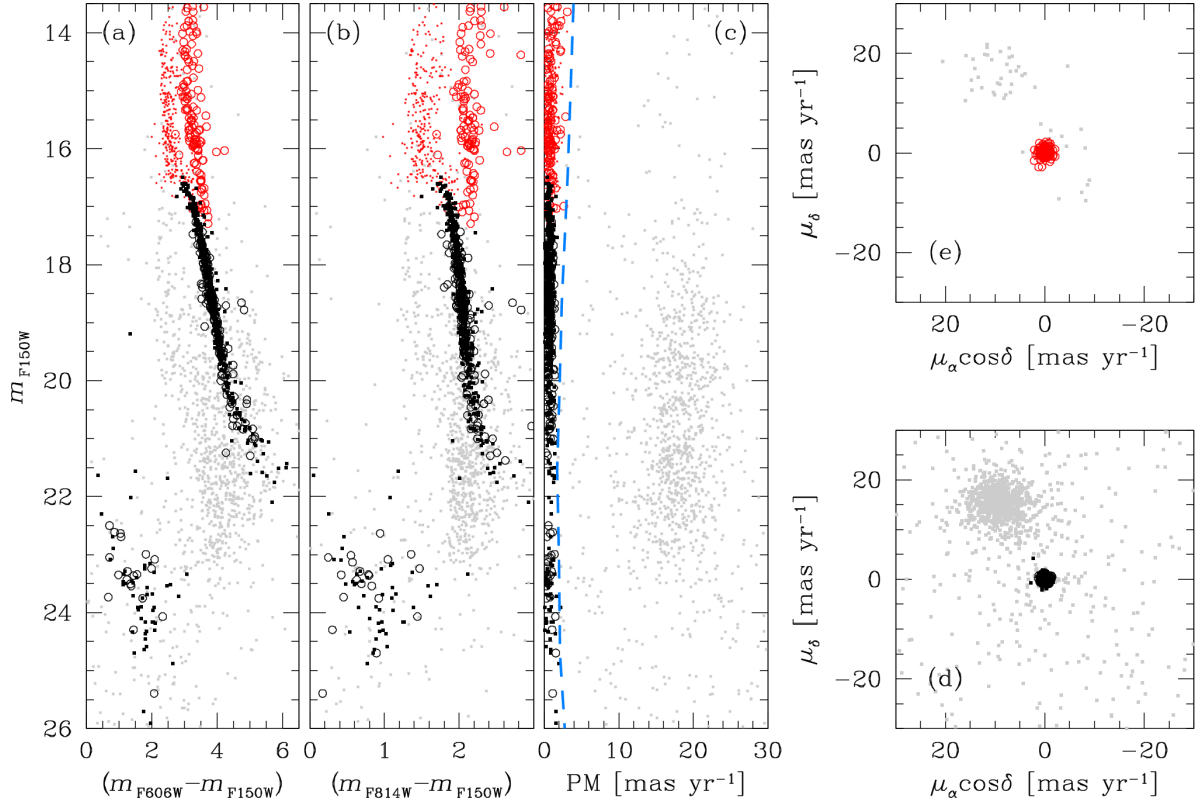
Fig. 2. Overview results for NGC 6121. Panels a and b present the m_{F150W} as a function of $(m_{F606W} - m_{F150W})$ and $(m_{F814W} - m_{F150W})$ CMDs, respectively. We plot m_{F150W} as a function of PM in panel c. In all these panels, gray points represent field stars, while all other colors refer to cluster members according to their PMs. Black open circles and dots are unsaturated stars measured in the Northern and Southern fields, respectively. The corresponding symbols in red mark saturated sources in NIRISS. The blue dashed line in panel c was used to infer cluster membership. Panels d and e show the VPD for unsaturated and saturated stars, respectively.

objects measured in the Northern and Southern NIRISS fields, respectively. The Northern and Southern fields have different read-out modes (NIS and NISRAPID, respectively) and therefore different behavior for saturated objects, which explains the discrepancy between the two cluster sequences in red. All other objects are plotted as gray points. The cluster membership is inferred by hand in the plot PM as a function of magnitude (blue dashed line in panel b of Fig. 2). This threshold is defined as the compromise between excluding field stars with cluster-like motion and including genuine cluster members. To take into account the larger PM errors of saturated and very faint stars, the membership criteria are less severe for these objects.

The photometry for saturated stars is still not reliable (red points in Fig. 2), as it creates unphysical blue/red turns in the CMDs, and is different for the two sets of NIRISS data. On the other hand, the PMs of saturated and unsaturated objects are in sufficient agreement with each other and are precise enough to assess the cluster membership (see panels d and e). These pieces of information might suggest that brighter-fatter effects have a more severe impact on the photometry of very bright sources rather than on their astrometry, at least for NIRISS.

The CMDs in Fig. 2 are corrected for a small zero-point (~0.05 mag) between the NIRISS photometry of unsaturated stars using the Northern- and Southern-field data. We do not know the reason for this offset, but we have corrected for it by applying the offset to the Southern-field data taken with the NIS-RAPID readout. We chose to correct the photometry of this data set because for both NGC 6121 and NGC 6397 we noticed a better agreement between our CMDs with NIRISS data taken

with the NIS readout and theoretical isochrones (Sect. 4). While differential reddening could also explain the discrepancy in the photometry of the two fields (the extinction in NGC 6121 varies significantly across the field, with $\Delta E(B - V)$~0.2; Hendricks et al. 2012), it is unlikely to be the cause, because this zero-point is not present in the F606W and F814W photometry.

The combination of HST and JWST data allows us to probe the MS of NGC 6121 down to $m_{F150W} \sim 22$ ($m_{F606W} \sim 27.5$). This depth is comparable with what was obtained by Bedin et al. (2009), who used F606W (and F775W) observations for their HST program GO-10146 that were about ten times longer (1200 s). However, we fall ~1 mag short with respect to Bedin et al. (2009) along the WD sequence.

3.2. NGC 6397

A CMD of NGC 6397 constructed with m_{F150W} as a function of $(m_{F775W} - m_{F150W})$ and corrected for differential reddening using $E(B - V)$=0.22 (Correnti et al. 2018) is presented in panel (a) of Fig. 3. As noted for NGC 6121, the astrometry of saturated stars seems consistent with that of unsaturated objects, whereas there is a clear systematic issue with the saturated-star photometry. We also note that a sample of background galaxies (green crosses in Fig. 3) was measured in both epochs. We used these galaxies to measure the absolute PM of the clusterm and the results are presented in Appendix A.

As for NGC 6121, we can measure stars along the MS of NGC 6397 down to $m_{F150W} \sim 23$. We can also probe the brightest
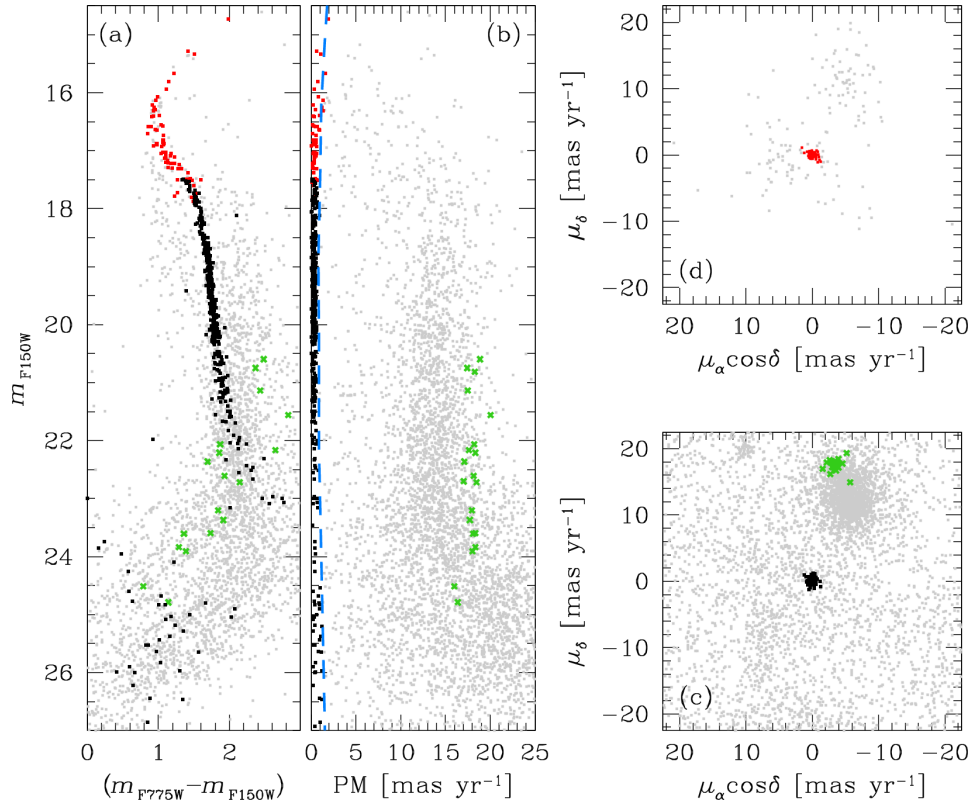
Fig. 3. Similar to Fig. 2 but for NGC 6397. The green crosses in panels a, b, and c refer to a sample of background galaxies selected from the NIRISS stacked image (see Appendix A for details). The clump of points in panel c at about $(\mu_\alpha \cos\delta, \mu_\delta) \sim (10, 20)$ mas yr^{-1} is caused by mismatches between residual PSF artifacts in the NIRISS data and real field stars in the HST catalog that moved by 11 pixels over 20 years.

part of the WD sequence, but we are again limited by the shallow HST data (see Appendix B).

4. Isochrone fitting

The following subsections describe the isochrone-fitting procedure for the two clusters. Hereafter, we consider only well-measured cluster members, that is, those objects that have: (i) a RADXS value (excess or deficiency of flux outside the core of the star compared to what was predicted by the ePSF; Bedin et al. 2008) within ±0.1; (ii) a fractional flux within the fitting radius prior to neighbor subtraction (e.g., Libralato et al. 2022) lower than 0.25; (iii) a flux at least 3σ above the local sky; (iv) a rejection rate (number of images where a source was measured over the number of images in which a source was found) of lower than 40%; and (v) a PM measurement. All CMDs presented in our work are corrected for the so-called input–output effect described in Appendix B.

4.1. NGC 6121

We compared our CMDs of NGC 6121 with model isochrones from the "a Bag of Stellar Tracks and Isochrones" (BaSTI-IAC, Hidalgo et al. 2018; Pietrinferni et al. 2021) and the "evolutionary extension to the Spectral Analog of Dwarfs" (SANDee, II) collections. In both cases, we chose the isochrones with [Fe/H] and [α/Fe] closest to the spectroscopic values in Marino et al. (2008): [Fe/H] = −1.07 and [α/Fe] = 0.39. We selected the isochrone with [Fe/H] = −1.1 and [α/Fe] = 0.35 from the SANDee grid.

We used the BaSTI web interpolator[11] to obtain an isochrone with [α/Fe] = 0.4 and the metal mass fraction, Z, set to the same value as that in the chosen SANDee isochrone ($Z = 0.002237$). In both cases, we used the age of 12 Gyr from Bedin et al. (2009) and the distance of 1.85 kpc from Baumgardt & Vasiliev (2021). The optical reddening, $E(B - V)$, was treated as a free parameter with temperature-dependent reddening corrections evaluated using the BasicATLAS (Larkin et al. 2023) software package and $R_V = 3.67$ (Hendricks et al. 2012). When calculating synthetic photometry, we adopted the net throughput curves of NIRISS[12], which include both the transmissivity of the filter and the optical train of the instrument. For ACS/WFC, we employed the instrument response curves from stsynphot[13].

As SANDee isochrones are only available at $T_{\text{eff}} \leq 4000$ K, we extended them to cover the entire range of available photometry by calculating additional model atmospheres using ATLAS-9 (Kurucz 2005, 2014; Kurucz & Avrett 1981) and evolutionary models using MESA (Paxton et al. 2011, 2013, 2015, 2018, 2019), following the procedure described in Gerasimov et al. (2024b). The two isochrones evaluated at the best-fit reddening are plotted in Figure 4. The best-fit reddening for each isochrone in each filter combination is indicated in the figure legend. Both isochrones suffer from two shortcomings:

1. The best-fit reddening, $E(B - V)$, exceeds the values in the previous studies of bright cluster members (e.g., $E(B - V) =$ 0.37 in Hendricks et al. 2012, $E(B - V) = 0.35$ in Harris 1996), by $\gtrsim 0.1$ mag. It must be noted that $E(B - V)$ varies

---

[11] http://basti-iac.oa-abruzzo.inaf.it/isocs.html
[12] See the dedicated JDox page
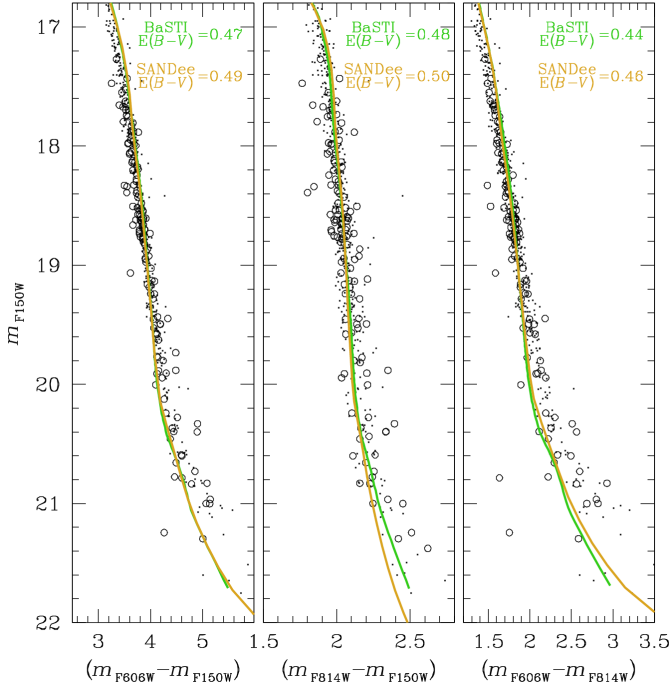[13] https://stsynphot.readthedocs.io/en/latest/

Fig. 4. Collection of CMDs for the MS of NGC 6121. Only well-measured cluster members are shown using the same symbols as in Fig. 2. The green and yellow lines represent the best-fit BaSTI and SANDee isochrones, respectively, using distance and metallicity from the literature. The best-fit extinction for each isochrone is provided in each panel.

Fig. 5. Goodness-of-fit parameter (χ^2) and the best-fit $E(B-V)$ for each isochrone tested in our work (see the text for details). The most accurate models are expected to have low χ^2, and best-fit $E(B-V)$ that are both comparable to the values inferred from bright members in the literature (0.3–0.4) and consistent across the three considered color combinations.

by up to 0.1 mag depending on the specific line of sight within the cluster (Hendricks et al. 2012), and the large best-fit $E(B-V)$ value derived in this work may be partly explained by above-average reddening in the observed field. Moreover, the NASA/IPAC Galactic Reddening service[14] suggests that $E(B-V)$ may be as high as 0.43 in the observed part of the cluster. However, the inferred $E(B-V)$ of ∼0.5 from the ($m_{F814W} - m_{F150W}$) CMD (middle panel of Figure 4) is still irreconcilable with optical estimates in the literature even for the most extreme lines of sight.

2. In all CMDs, at faint magnitudes ($m_{F150W} \gtrsim 20$) the observed color–magnitude trend appears redder than the colors predicted by the best-fit isochrones.

To determine the origin of these discrepancies, we investigated a wide variety of possible causes by recalculating the SANDee isochrone with alternative parameters. For all test isochrones, the goodness-of-fit value and the best-fit reddening are plotted in Figure 5. The test isochrones that differ the most from the nominal model are overplotted on the observed photometry in Figure 6. The following possible explanations for the observed discrepancy were explored:

1. Reduced oxygen abundance. Globular clusters are characterized by the oxygen-sodium anti-correlation (Peterson 1980), with oxygen-deficient stars typically comprising the majority of members (Bastian & Lardo 2015). At low effective temperatures, [O/Fe] controls the abundance of water vapor that produces prominent absorption bands in the infrared. We calculated two test isochrones with [O/Fe] = 0.0 and [O/Fe] = −0.2 (we note that the nominal abundance of oxygen is [O/Fe]=[α/Fe]=0.35). Both isochrones display more
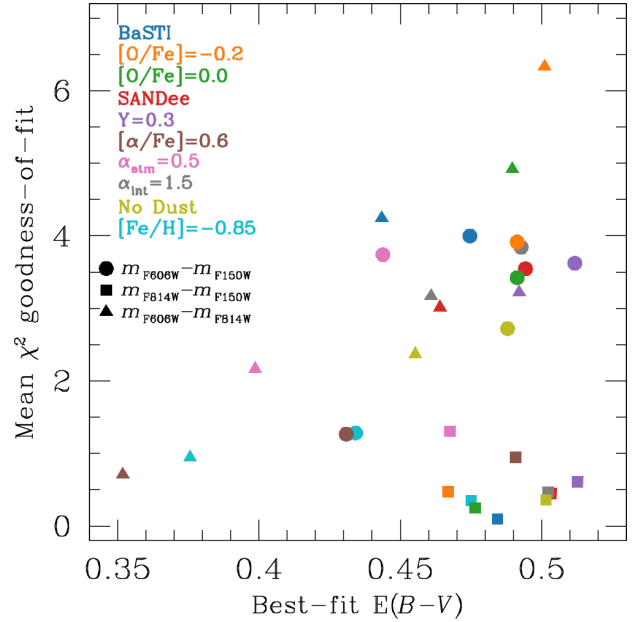
aggressive reddening of the lower MS in ($m_{F814W} - m_{F150W}$), as expected. However, the fit is much worse in ($m_{F606W} - m_{F814W}$), as these bands do not overlap with major H_2O absorption bands, and the reduced average opacity of the atmosphere increases its effective temperature, making the optical color bluer. The oxygen abundance therefore cannot explain the observed discrepancy on its own, but it may be able to do so in conjunction with another effect that compensates for the decrease in the average opacity.

2. Increased α-enhancement or metallicity. We compared our CMDs to the SANDee isochrone with [Fe/H] = −0.85 (0.25 dex more metal-rich than the nominal case) and computed a test isochrone with [α/Fe] = 0.6 (0.25 dex more α-enhanced than the nominal case). The effects of both metallicity and α-enhancement on the observed CMD are similar: they increase the average atmospheric opacity, resulting in a reduction in the effective temperature and redder colors. The only exception is the effect of [α/Fe] in ($m_{F814W} - m_{F150W}$), where the influence of absorption bands within the filter wavelengths dominates over the effect of average opacity, resulting in a slightly bluer color than the nominal SANDee isochrone. Both test isochrones yield a better fit to the data and a lower value of $E(B-V)$ in accordance with the literature. If the increased metallicity and/or α-enhancement is indeed responsible for the observed reddening of the lower MS, the atmospheric composition must be varying with stellar mass in order to remain consistent with the spectroscopic chemistry inferred from observations of higher-mass members. We also note that increasing [Fe/H] or [α/Fe] appears to increase the scatter in the best-fit $E(B-V)$ values among our CMDs (see Figure 5), suggesting that [Fe/H] and [α/Fe] adjustments are not sufficient to explain the discrepancy on their own.

3. Increased helium mass fraction. The nominal SANDee isochrone adopts the helium mass fraction of $Y = 0.25$. We

---

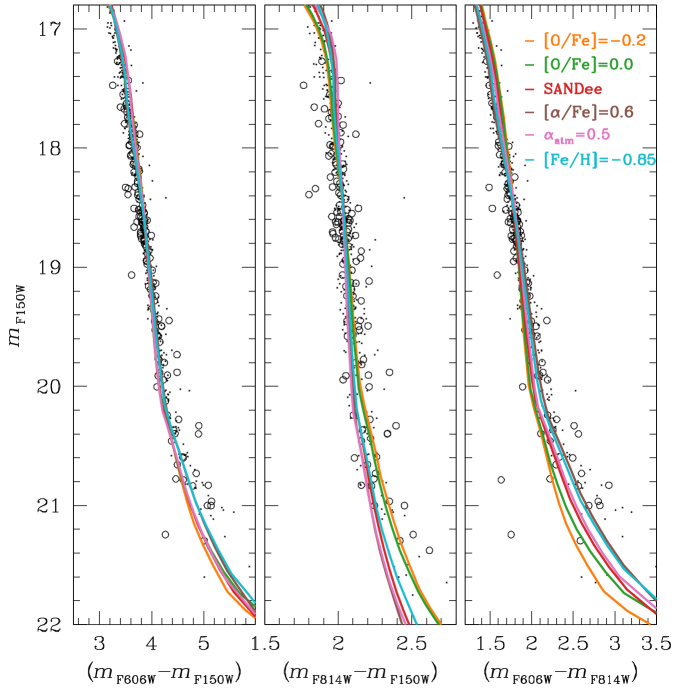[14] https://irsa.ipac.caltech.edu/applications/DUST/

Fig. 6. Selected alternative isochrone fits that are most different from the nominal SANDee isochrone shown in Fig. 4. The nominal isochrone is shown in gray for reference. Depending on the filter combination, some SANDee isochrones provide a good fit to the observed CMD, even at the faint-end of the MS, but no isochrone can capture all features in all three CMDs.

calculated a test isochrone with $Y = 0.3$ to evaluate the effect of helium content on stellar evolution. The effect of the helium mass fraction on the lower main sequence is comparatively small and mostly degenerate with the effect of stellar mass. It therefore cannot be observed in the CMD. On the upper main sequence and near the turn-off point, higher Y results in bluer colors and a correspondingly higher best-fit value of $E(B - V)$, exacerbating the discrepancy.

4. Convective mixing length. In SANDee model isochrones, convective transfer in both stellar interiors and atmospheres is treated in the formalism of the mixing-length theory (Böhm-Vitense 1958). In stellar interiors, the mixing length of $\alpha_{int} = 1.82$ scale heights is adopted, which is based on the solar calibration in Salaris & Cassisi (2015). In stellar atmospheres, SANDee employs a mixing length formula from Ludwig et al. (1999) derived from radiation hydrodynamics simulations. In the ATLAS models calculated in this study to extend SANDee to $T_{eff} > 4000$ K, we kept the default ATLAS atmospheric mixing length of $\alpha_{atm} = 1.25$ scale heights, which is inferred from the solar calibration (Kurucz 1992). To investigate the effect of convection on the isochrone, we computed two test isochrones with $\alpha_{int} = 1.5$ and $\alpha_{atm} = 0.5$. Changing the interior mixing length does not noticeably alter the isochrone below the MS turn-off, and cannot explain the observed discrepancies. Reducing the atmospheric mixing length impacts the atmospheric structure in a similar way to increased metallicity or α-enhancement; however, the magnitudes of these effects are only comparable near $T_{eff} \sim 4000$ K. At lower temperatures, where we see the largest discrepancy between the data and the model, the effect of convective mixing length is much smaller and cannot explain our observations.

5. Dust condensation. In the atmospheres of cool stars and brown dwarfs, liquid and solid species may condense out of the gaseous form, offsetting the chemical equilibrium and altering the spectral energy distribution. In SANDee, at the range of T_{eff} considered in this study, dust condensation is treated using the inefficient settling (equilibrium) model from Allard et al. (2001). We calculated an additional test isochrone without dust condensation. While the dust-free isochrone predicts redder colors at the lowest effective temperatures, the effect of condensation at the low metallicity of the cluster and the comparatively warm temperatures of stars within our photometric limit ($T_{eff} > 3000$ K) is not sufficient to account for the observed discrepancy.

The tests described above suggest that it may be possible to reconcile the observed CMDs and theoretical models by simultaneously reducing the oxygen abundance by ∼0.4 dex in low-mass stars to capture the unexpectedly large reddening of the ($m_{F814W} - m_{F150W}$) color near the end of the MS, and increasing the average opacity of the atmosphere to reduce the effective temperatures of low-mass stars. The latter effect is most readily attained by increasing [Fe/H] and/or [α/Fe] by ∼0.3 dex, and may be indicative of incomplete opacities in the model atmospheres. However, this seems unlikely, as the effect is consistent across multiple modeling codes, and persists into relatively high temperatures of $T_{eff} \gtrsim 4000$ K, where the opacity model is more straightforward. Other effects such as dust condensation, helium enhancement and convection cannot explain the observed discrepancy.

If not in the isochrones, the problem may reside in the data, although we do not find any clear systematic issue that can explain the discrepancies. Possible speculations include color-dependent systematics or a second-order by-product of the brighter-fatter effect. For the latter case, the NIRISS ePSFs are made using bright stars that might partially be affected by the brighter-fatter effect (although specific magnitude thresholds were adopted in the ePSF modeling to avoid this issue; Libralato et al. 2023). The faintest stars in our CMDs, which instead are not impacted by the brighter-fatter issue, could result in small magnitude-dependent systematics when fitted with these ePSFs, given that the ePSFs are not the real representation of the flux distribution of such faint sources. The main flaw in this hypothesis is the good agreement between the photometry of the Northern and Southern fields, which were taken with different readout patterns and exposure times and hence are impacted differently by the brighter-fatter phenomenon.

From the physical side, a possible explanation could be that, at the faint end of our CMDs, the points are not redder than the canonical theoretical tracks but brighter, and these brighter sources are just MS binaries made by very-low-mass MS stars. However, it is unclear as to why such objects should comprise the majority of the sources at these magnitudes and which dynamical processes could preferably retain them at the clustercentric distance of our fields. A future analysis of the NIRCam data of NGC 6121 will allow us to shed more shed light on the topic.

4.2. NGC 6397

For NGC 6397, we followed the procedure in Gerasimov et al. (2024b) to calculate two model isochrones: a nominal isochrone with parameters matching the literature, and a corrected isochrone with adjusted [Fe/H], [α/Fe] and [O/Fe] to attain the best correspondence between the model and the data. For the nominal isochrone, we adopted the median abundances of elements from Milone et al. (2012a) ([C/Fe] = 0.03, [N/Fe] = 0.58,
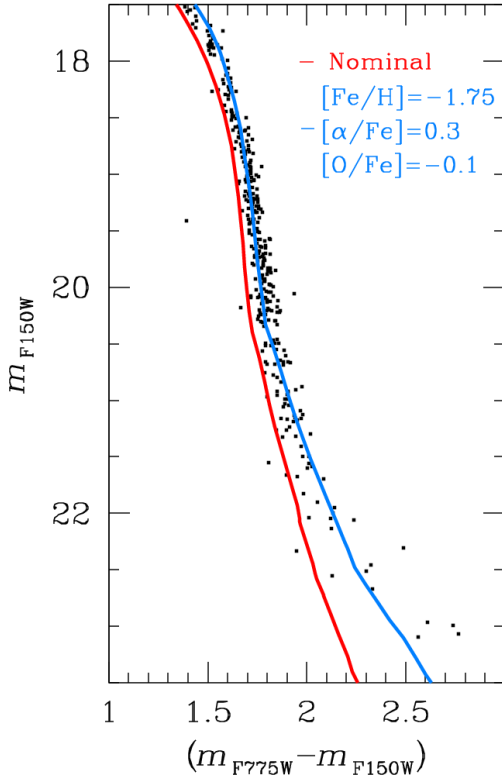
Fig. 7. CMD for the MS of NGC 6397. The red line represents an isochrone with nominal parameters from the literature, whereas the blue line shows the adjusted option that provides the best fit to the data (see the text for details).

[O/Fe] = 0.28), age of 13.5 Gyr from beryllium dating in Pasquini et al. (2004), metallicity of [Fe/H] = −1.88, distance modulus of 12.02, and reddening of $E(B − V) = 0.22$ from Correnti et al. (2018), and $R_V = 3.1$. As seen in Fig. 7, the nominal isochrone suffers from the same shortcomings as the nominal isochrones of NGC 6121: it appears consistently bluer than the data across the entire observed mass range, and fails to reproduce the rapid reddening of the CMD at $m_{\rm F150W} \gtrsim 21$.

We attempted to correct the nominal isochrone by introducing similar offsets to its parameters, as inferred in the case of NGC 6121. Namely, we reduced [O/Fe] by ∼0.4 dex to [O/Fe] = −0.1 and increased [α/Fe] by 0.3 dex. We then increased the metallicity to [Fe/H] = −1.75 to resolve the remaining discrepancy in color. This corrected isochrone provides a better fit to the data. However, similarly to the case of NGC 6121, we find that the corrected isochrone does not fully reproduce the red turn at the bottom of the main sequence. As discussed in the previous section, we do not know whether this is a real feature – the ingredients of which are not properly included in the current theoretical tracks – or a product of a systematic in the data.

4.3. The WD cooling sequence

Figure 8 zooms onto the WD region to show a comparison with a set of BaSTI WD isochrones (Salaris et al. 2010). The reddening, age, and distance modulus are the same as in Figs. 4 and 7. The limited depth of the HST data (see Appendix B) makes it possible to study only the bright part of the WD sequence, that is, WDs with a mass of ∼0.55 $M_\odot$. Nevertheless, there is a good agreement between the observed sequence and the theoretical track.

5. Luminosity and mass functions

Thanks to the PM-cleaned CMDs made by combining HST and JWST data, we studied the MS of the clusters down to <0.1 $M_\odot$ and computed the present-day local LFs and MFs of the two clusters. The LF and MF of a stellar population provide useful insights about the formation and dynamical evolution of the system (e.g., Vesperini & Heggie 1997).

The LF of each cluster was obtained as follows. We selected a sample of well-measured (see Sect. 4) MS stars, divided it into bins of 1 mag in width (with steps of 0.5 mag) and counted the number of sources in each bin. The number of stars per bin was corrected for completeness using the outputs of the artificial-star tests described in Appendix B. Finally, we normalized the number of stars by the total area in arcmin^2 of the overlapping HST and JWST fields. This way, we can directly compare the LFs of the two clusters, and also cross-checked the photometry of the Northern and Southern fields of NGC 6121 again, which were analyzed independently. The present-day local LFs of NGC 6121 and NGC 6397 are shown in the bottom panels of Fig. 9. The field contamination can be a source of uncertainty when computing the LF of a cluster. However, these two systems are the closest GCs to the Sun, and the separation between cluster and field objects in the VPD was found to be clear even at the faintest magnitudes; we neglected the contribution of the field contamination.

Thanks to the isochrones described in Sect. 4, we were able to compute the present-day local MFs in a similar fashion. We converted the F150W-filter magnitudes in masses using the isochrones and counted the number of stars in bins of 0.1 $M_\odot$ in width with steps of 0.05 $M_\odot$. As for the LFs, the number of stars was corrected for completeness and normalized by the area of the field. The result is shown in the top panels of Fig. 9. Both clusters show a change of slope in the MFs. For NGC 6121, the break point happens at ∼0.3–0.4 $M_\odot$. For NGC 6397, the slope change is slightly below 0.2 $M_\odot$. We report the values of the LFs and MFs for the two clusters in Tables 1 and 2.

We measured the slope α of the present-day local MFs[15] by fitting a straight line to the all mass bins in Fig. 9 and found:
- NGC 6121 (0.1<M<0.6 $M_\odot$): $\alpha_{@3.6\,\rm arcmin} = 0.40 \pm 0.29$;
- NGC 6121 (0.1<M<0.6 $M_\odot$): $\alpha_{@4.8\,\rm arcmin} = 0.47 \pm 0.18$;
- NGC 6397 (0.07<M<0.5 $M_\odot$): $\alpha_{@11.5\,\rm arcmin} = -0.14 \pm 0.26$.

For both clusters, the measured slopes are significantly flatter than the values expected in the observed mass range for a Salpeter (1955, $\alpha^{\rm Salpeter} = -2.35$) or a Kroupa (2001, $\alpha^{\rm Kroupa} = -1.3$) stellar MF. A flattening of the global stellar MF is the expected consequence of the preferential loss of low-mass stars due to the effects of two-body relaxation (see, e.g., Vesperini & Heggie 1997). For the interpretation of the observed values of the slope of the MF, however, it is important to consider that effects other than the stellar escape can alter the global slope of the MF. For example, two-body relaxation causes massive stars to segregate in the cluster's inner regions and low-mass stars to migrate outwards, leading to a variation of the MF slope with the distance from the cluster center. As massive stars migrate inwards and low-mass stars outwards, the slope of the MF in the inner (outer) regions becomes flatter (steeper) than the global one (Vesperini & Heggie 1997). We refer to, for example, King et al. (1995) for an early HST study of the radial variation of the MF in NGC 6397, or the recent study by Baumgardt et al. (2023, and its online database) for the radial variation of the MF in GCs.

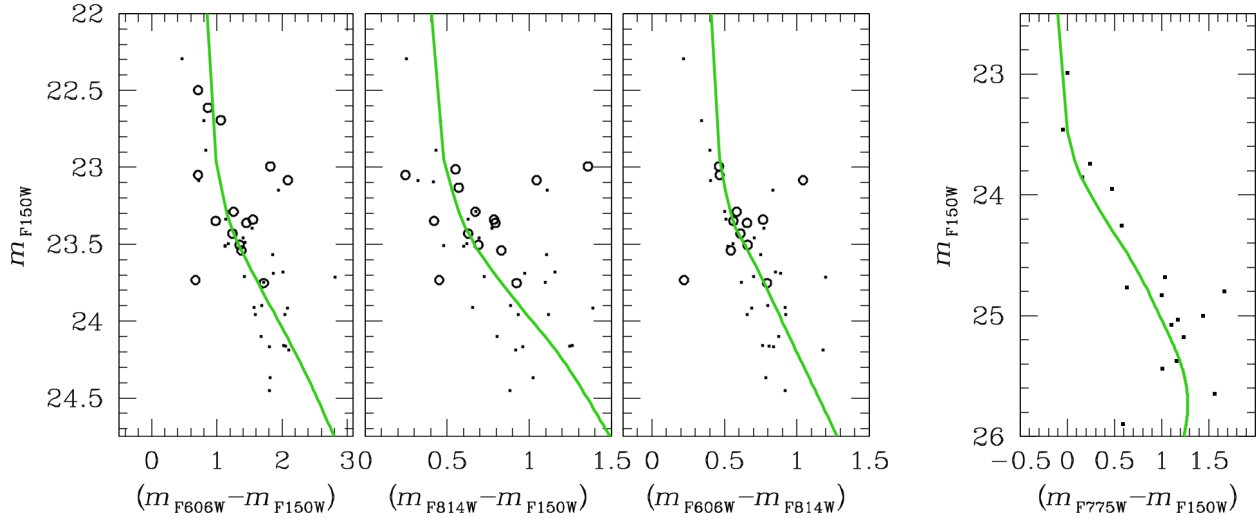[15] We consider the expression $N(m) \propto m^\alpha$, i.e., $\alpha = -2.35$ for a Salpeter MF.

Fig. 8. Collection of CMDs focused on the WD sequence of NGC 6121 (three leftmost panels) and NGC 6397 (rightmost panel). Only well-measured cluster members are shown. For NGC 6121, we use the same symbols as in the previous figures. A BaSTI WD isochrone is shown in each plot (green line).

Table 1. LF and MF for NGC 6121.

m_{F150W}	Northern field		Southern field	
	N^* arcmin^{-2}	Error	N^* arcmin^{-2}	Error
16.75			4.00	2.00
17.25			9.08	3.01
17.75	7.25	2.69	9.26	3.04
18.25	8.10	2.85	10.69	3.27
18.75	16.02	4.00	12.42	3.52
19.25	6.12	2.47	8.16	2.86
19.75	4.52	2.13	4.24	2.06
20.25	4.22	2.05	3.36	1.83
20.75	4.64	2.15	2.26	1.50
21.25	2.75	1.66	1.45	1.21
21.75			0.88	0.94
22.25			0.34	0.59
$M\,(M_\odot)$	N^* arcmin^{-2}	Error	N^* arcmin^{-2}	Error
0.10	3.20	1.79	2.37	1.54
0.15	7.88	2.81	5.42	2.33
0.20	5.43	2.33	4.38	2.09
0.25	4.81	2.19	7.09	2.66
0.30	5.68	2.38	6.81	2.61
0.35	12.01	3.47	8.29	2.88
0.40	7.26	2.69	8.54	2.92
0.45	6.88	2.62	8.32	2.88
0.50			8.54	2.92
0.55			4.81	2.19

Table 2. LF and MF for NGC 6397.

m_{F150W}	N^* arcmin^{-2}	Error
17.75	2.95	1.72
18.25	3.24	1.80
18.75	4.67	2.16
19.25	6.11	2.47
19.75	5.76	2.40
20.25	4.83	2.20
20.75	2.91	1.71
21.25	2.20	1.48
21.75	1.18	1.08
22.25	0.77	0.87
22.75	0.57	0.75
23.25	0.24	0.49
$M\,(M_\odot)$	N^* arcmin^{-2}	Error
0.075	1.55	1.25
0.125	4.81	2.19
0.175	6.07	2.46
0.225	5.14	2.27
0.275	3.48	1.87
0.325	3.77	1.94
0.375	4.16	2.04
0.425	3.14	1.77
0.475	2.34	1.53

The values of α found in NGC 6121 and NGC 6397 are the result of all these processes affecting both the global and the local MF. The location of the fields for NGC 6121 and that of NGC 6397 correspond, respectively, to an intermediate region of the clusters for NGC 6121 (about 0.8 r_h and 1 r_h for Northern and Southern fields, respectively) and an outer region for NGC 6397 (at about 4r_h from the cluster's center). Part of the difference between the observed slope of the MF in NGC 6121 and NGC 6397 is therefore due to the different regions observed for the two clusters and is consistent with the expected trend between the slope and the distance from the cluster center. Part of the difference may also be due to differences between the global MFs of the two clusters. For both clusters, the flat values of the slope of the MF revealed by our observations suggest that these systems have been significantly affected by mass loss and the preferential escape of low-mass stars. This conclusion is in agreement with the results of a number of previous studies wherein specific N-body and Monte Carlo evolutionary models were built for these two clusters (Heggie & Giersz 2008; Hurley et al. 2008; Giersz & Heggie 2009).
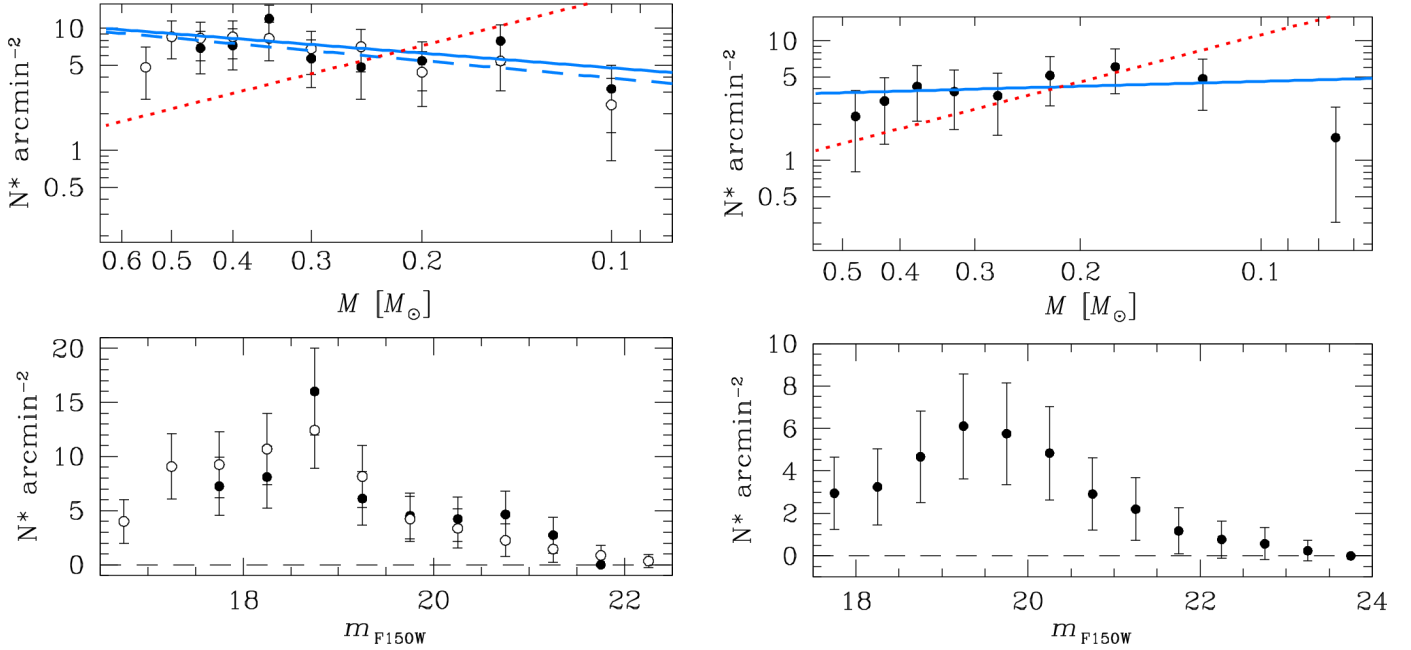
Fig. 9. Present-day local LFs (bottom panels) and MFs (top panels) for NGC 6121 (left column) and NGC 6397 (right column). Error bars represent the propagated Poisson errors. The horizontal, dashed line in the bottom panels is set to zero for reference. For NGC 6121, we plot the results for the Northern and Southern fields with open and filled dots, respectively. In the top panels, the blue lines represent straight-line fits to the points, the slopes of which are reported in the text. For the case of NGC 6121, the blue solid line refers to the Northern field, while the dashed line is obtained from the Southern-field points. Finally, the red, dotted lines have a slope of −1.3 (i.e., that of a Kroupa MF in the observed mass range) and arbitrary intercept to fit in the plot.

6. Discussion and conclusions

The JWST is ideal for studying low-mass stars because they are faint and red objects, and are brighter at longer wavelengths than their more-massive counterparts, which makes them ideal targets for near-infrared observations. Since the launch of JWST, an increasing number of authors have begun to focus on faint stars in GCs. Our paper is the fourth in a series investigating the faintest members of NGC 6121 and NGC 6397, the two geometrically closest GCs to us. In this study, we analyzed the parallel fields observed with the NIRISS detector of JWST.

We discuss the data reduction of the NIRISS data, from the pipeline setup to the extraction of accurate and precise positions and fluxes for all sources in the field. We demonstrate that, in combination with archival HST data, it is possible to clearly disentangle cluster members from field stars down to <0.1 $M_\odot$. The NIRISS data alone have the potential to probe even fainter stars along the MS but the HST data limit the complete exploitation of the information provided by JWST. Future follow ups with JWST will allow us to potentially investigate stars down to the hydrogen-burning limit, as done for the same clusters with the NIRCam data in the primary fields of this project.

We compare the observed CMDs with theoretical isochrones. While there is a good agreement on the brighter part of the MS, the faint-end of the MS is not reproduced by the theoretical tracks using literature values for the extinction and chemical composition. Only models with higher reddening and/or metallicity are able to fit the red turn of the MS. We discuss various hypotheses that might explain these findings, from shortcomings in the isochrones to systematics in the data.

Finally, we compute the LFs and MFs for the two clusters. The slopes of the MF are measured close to the r_h for NGC 6121 and in the outer regions at about $4r_h$ for NGC 6397. The differences between the slopes found for the two clusters are generally consistent with the expected effects associated with the spatial outward (inward) migration of low-mass (high-mass) stars due to two-body relaxation (differences between the global MFs of the two clusters could also be in part responsible for the observed differences between the local MFs). In general, our observations reveal a significant flattening in the MF that indicates that, for both of these clusters, the present-day MF has been significantly affected by the preferential loss of low-mass stars.

Data availability

As part of this publication, we release the star catalogs (positions, photometry, and membership) and the astrometrized stacked images through the CDS and our website[16]. A description of this supplementary online electronic material is provided in Appendix C.

Astro-photometric catalogs and stacked images are available at the CDS via anonymous ftp to `cdsarc.cds.unistra.fr` (`130.79.128.5`) or via `https://cdsarc.cds.unistra.fr/viz-bin/cat/J/A+A/690/A371`.

---

[16] `https://web.oapd.inaf.it/bedin/files/PAPERs_eMATERI-ALs/JWST/GO-1979/P04/`

References

Allard, F., Hauschildt, P. H., Alexander, D. R., Tamanai, A., & Schweitzer, A. 2001, ApJ, 556, 357

Anderson, J., & King, I. R. 2006, PSFs, Photometry, and Astronomy for the ACS/WFC, Instrument Science Report ACS 2006-01

Anderson, J., & Ryon, J. E. 2018, Improving the Pixel-Based CTE-correction Model for ACS/WFC, Instrument Science Report ACS 2018-04, 37

Astropy Collaboration (Robitaille, T. P., et al.) 2013, A&A, 558, A33

Astropy Collaboration (Price-Whelan, A. M., et al.) 2018, AJ, 156, 123

Bastian, N., & Lardo, C. 2015, MNRAS, 453, 357

Bastian, N., & Lardo, C. 2018, ARA&A, 56, 83

Baumgardt, H., & Sollima, S. 2017, MNRAS, 472, 744

Baumgardt, H., & Vasiliev, E. 2021, MNRAS, 505, 5957

Baumgardt, H., Hénault-Brunet, V., Dickson, N., & Sollima, A. 2023, MNRAS, 521, 3991

Bedin, L. R., King, I. R., Anderson, J., et al. 2008, ApJ, 678, 1279

Bedin, L. R., Salaris, M., Piotto, G., et al. 2009, ApJ, 697, 965

Bedin, L. R., Salaris, M., Anderson, J., et al. 2019, MNRAS, 488, 3857

Bedin, L. R., Nardiello, D., Salaris, M., et al. 2024, Astron. Nachr., 345, e20240039

Bellini, A., Anderson, J., van der Marel, R. P., et al. 2014, ApJ, 797, 115

Bellini, A., Anderson, J., Bedin, L. R., et al. 2017a, ApJ, 842, 6

Bellini, A., Anderson, J., van der Marel, R. P., et al. 2017b, ApJ, 842, 7

Bianchini, P., van der Marel, R. P., del Pino, A., et al. 2018, MNRAS, 481, 2125

Böhm-Vitense, E. 1958, Z. Astrophys., 46, 108

Burgasser, A. J. 2004, ApJS, 155, 191

Burgasser, A. J., Kirkpatrick, J. D., Reid, I. N., et al. 2003, ApJ, 586, 512

Bushouse, H., Eisenhamer, J., Dencheva, N., et al. 2023, https://doi.org/10.5281/zenodo.6984365

Cadelano, M., Pallanca, C., Dalessandro, E., et al. 2023, A&A, 679, L13

Calamari, E., Faherty, J. K., Burningham, B., et al. 2022, ApJ, 940, 164

Carretta, E., Gratton, R. G., Clementini, G., & Fusi Pecci, F. 2000, ApJ, 533, 215

Cassisi, S., & Salaris, M. 2020, A&A Rev., 28, 5

Correnti, M., Gennaro, M., Kalirai, J. S., Cohen, R. E., & Brown, T. M. 2018, ApJ, 864, 147

Dieball, A., Bedin, L. R., Knigge, C., et al. 2016, ApJ, 817, 48

Dieball, A., Bedin, L. R., Knigge, C., et al. 2019, MNRAS, 486, 2254

Dotter, A., Ferguson, J. W., Conroy, C., et al. 2015, MNRAS, 446, 1641

Doyon, R., Hutchings, J. B., Beaulieu, M., et al. 2012, SPIE Conf. Ser., 8442, 84422R

Gaia Collaboration (Prusti, T., et al.) 2016, A&A, 595, A1

Gaia Collaboration (Brown, A. G. A., et al.) 2021, A&A, 649, A1

Gardner, J. P., Mather, J. C., Abbott, R., et al. 2023, PASP, 135, 068001

Gerasimov, R., Burgasser, A. J., Homeier, D., et al. 2022a, ApJ, 930, 24

Gerasimov, R., Burgasser, A. J., Homeier, D., et al. 2022b, in The 21st Cambridge Workshop on Cool Stars, Stellar Systems, and the Sun, Cambridge Workshop on Cool Stars, Stellar Systems, and the Sun, 120

Gerasimov, R., Bedin, L. R., Burgasser, A. J., et al. 2024a, ApJ, 971, 65

Gerasimov, R., Burgasser, A. J., Caiazzo, I., et al. 2024b, ApJ, 961, 139

Giersz, M., & Heggie, D. C. 2009, MNRAS, 395, 1173

Goudfrooij, P., Grumm, D., Volk, K., et al. 2024, PASP, 136, 014503

Grieves, N., Bouchy, F., Lendl, M., et al. 2021, A&A, 652, A127

Harris, W. E. 1996, AJ, 112, 1487

Hayashi, C., & Nakano, T. 1963, Prog. Theor. Phys., 30, 460

Heggie, D. C., & Giersz, M. 2008, MNRAS, 389, 1858

Hendricks, B., Stetson, P. B., VandenBerg, D. A., & Dall'Ora, M. 2012, AJ, 144, 25

Hidalgo, S. L., Pietrinferni, A., Cassisi, S., et al. 2018, ApJ, 856, 125

Hilker, M., Baumgardt, H., Sollima, A., & Bellini, A. 2020, in Star Clusters: From the Milky Way to the Early Universe, 351, eds. A. Bragaglia, M. Davies, A. Sills, & E. Vesperini, 451

Hurley, J. R., Shara, M. M., Richer, H. B., et al. 2008, AJ, 135, 2129

King, I. R., Sosin, C., & Cool, A. M. 1995, ApJ, 452, L33

Kroupa, P. 2001, MNRAS, 322, 231

Kumar, S. S. 1962, AJ, 67, 579

Kurucz, R. L. 1992, in The Stellar Populations of Galaxies, 149, eds. B. Barbuy, & A. Renzini, 225

Kurucz, R. L. 2005, Mem. Soc. Astron. Ital. Suppl., 8, 14

Kurucz, R. L. 2014, Model Atmosphere Codes: ATLAS12 and ATLAS9 (Springer International Publishing), 39

Kurucz, R. L., & Avrett, E. H. 1981, SAO Special Report, 391

Larkin, M. M., Gerasimov, R., & Burgasser, A. J. 2023, AJ, 165, 2

Libralato, M., Bellini, A., Bedin, L. R., et al. 2018, ApJ, 854, 45

Libralato, M., Bellini, A., Vesperini, E., et al. 2022, ApJ, 934, 150

Libralato, M., Bellini, A., van der Marel, R. P., et al. 2023, ApJ, 950, 101

Libralato, M., Argyriou, I., Dicken, D., et al. 2024, PASP, 136, 034502

Ludwig, H.-G., Freytag, B., & Steffen, M. 1999, A&A, 346, 111

Luhman, K. L. 2012, ARA&A, 50, 65

Marino, A. F., Villanova, S., Piotto, G., et al. 2008, A&A, 490, 625

Marino, A. F., Milone, A. P., Legnardi, M. V., et al. 2024, ApJ, 965, 189

Marley, M. S., Seager, S., Saumon, D., et al. 2002, ApJ, 568, 335

Massari, D., Bellini, A., Ferraro, F. R., et al. 2013, ApJ, 779, 81

Milone, A. P., & Marino, A. F. 2022, Universe, 8, 359

Milone, A. P., Villanova, S., Bedin, L. R., et al. 2006, A&A, 456, 517

Milone, A. P., Marino, A. F., Piotto, G., et al. 2012a, ApJ, 745, 27

Milone, A. P., Piotto, G., Bedin, L. R., et al. 2012b, A&A, 540, A16

Milone, A. P., Marino, A. F., Bedin, L. R., et al. 2019, MNRAS, 484, 4046

Milone, A. P., Marino, A. F., Dotter, A., et al. 2023, MNRAS, 522, 2429

Nardiello, D., Bedin, L. R., Griggio, M., et al. 2023a, MNRAS, 525, 2585

Nardiello, D., Griggio, M., & Bedin, L. R. 2023b, MNRAS, 521, L39

Pasquini, L., Bonifacio, P., Randich, S., Galli, D., & Gratton, R. G. 2004, A&A, 426, 651

Paust, N. E. Q., Reid, I. N., Piotto, G., et al. 2010, AJ, 139, 476

Paxton, B., Bildsten, L., Dotter, A., et al. 2011, ApJS, 192, 3

Paxton, B., Cantiello, M., Arras, P., et al. 2013, ApJS, 208, 4

Paxton, B., Marchant, P., Schwab, J., et al. 2015, ApJS, 220, 15

Paxton, B., Schwab, J., Bauer, E. B., et al. 2018, ApJS, 234, 34

Paxton, B., Smolec, R., Schwab, J., et al. 2019, ApJS, 243, 10

Perrin, M. D., Soummer, R., Elliott, E. M., Lallo, M. D., & Sivaramakrishnan, A. 2012, SPIE Conf. Ser., 8442, 84423D

Perrin, M. D., Sivaramakrishnan, A., Lajoie, C.-P., et al. 2014, SPIE Conf. Ser., 9143, 91433X

Peterson, R. C. 1980, ApJ, 237, L87

Pietrinferni, A., Hidalgo, S., Cassisi, S., et al. 2021, ApJ, 908, 102

Renzini, A., D'Antona, F., Cassisi, S., et al. 2015, MNRAS, 454, 4197

Richer, H. B., Dotter, A., Hurley, J., et al. 2008, AJ, 135, 2141

Rieke, M. J., Kelly, D. M., Misselt, K., et al. 2023, PASP, 135, 028001

Salaris, M., & Cassisi, S. 2015, A&A, 577, A60

Salaris, M., Cassisi, S., Pietrinferni, A., Kowalski, P. M., & Isern, J. 2010, ApJ, 716, 1241

Salpeter, E. E. 1955, ApJ, 121, 161

Scalco, M., Gerasimov, R., Bedin, L. R., et al. 2024a, Astron. Nachr., 345, e20240018

Scalco, M., Libralato, M., Gerasimov, R., et al. 2024b, A&A, 689, A59

Sollima, A., & Baumgardt, H. 2017, MNRAS, 471, 3668

Thies, I., & Kroupa, P. 2007, ApJ, 671, 767

Thies, I., Pflamm-Altenburg, J., Kroupa, P., & Marks, M. 2015, ApJ, 800, 72

van der Marel, R. P., Alves, D. R., Hardy, E., & Suntzeff, N. B. 2002, AJ, 124, 2639

VandenBerg, D. A., Brogaard, K., Leaman, R., & Casagrande, L. 2013, ApJ, 775, 134

Vasiliev, E., & Baumgardt, H. 2021, MNRAS, 505, 5978

Vesperini, E., & Heggie, D. C. 1997, MNRAS, 289, 898

Webb, J. J., & Leigh, N. W. C. 2015, MNRAS, 453, 3278

Ziliotto, T., Milone, A., Marino, A. F., et al. 2023, ApJ, 953, 62

Appendix A: The absolute PM of NGC 6397

The many background galaxies clearly visible in both the HST and JWST stacked images of NGC 6397 offer us the opportunity to estimate the absolute PM of the cluster (e.g., Milone et al. 2006; Massari et al. 2013; Libralato et al. 2018). This simple exercise is meant to show the goodness of our data reduction and another example of the astrometric potential of the HST-JWST duo.

We identified by eye a sample of 20 background galaxies with a point-like core in the NIRISS stacked images. These sources are tightly distributed in the VPD (green crosses in Fig. 3). The 3σ-clipped median value of the PM in each coordinate of these sources, with opposite sign, is the absolute PM of the cluster in our NIRISS field:

$$(\mu_\alpha \cos\delta, \mu_\delta)_{@\text{Field}} = (3.309 \pm 0.145, -17.742 \pm 0.132) \text{ mas yr}^{-1}.$$

Our field is ~11.5 arcmin away from the center of NGC 6397, so the estimate above needs to be corrected by the projection effects that arise from the different line of sight between our analyzed field and the center of mass (COM) of the cluster. Using the equations provided in van der Marel et al. (2002) and assuming the position of our field and of the cluster's center described in Sect. 2, we obtain:

$$(\mu_\alpha \cos\delta, \mu_\delta)_{\text{COM}} = (3.257 \pm 0.145, -17.750 \pm 0.132) \text{ mas yr}^{-1}.$$

The rotation in the plane of the sky of NGC 6397 is small (e.g., Bianchini et al. 2018; Vasiliev & Baumgardt 2021), so we neglected its contribution. Our estimate of the absolute PM of the COM is in agreement with that from the *Gaia* DR3 provided in the GC database of Holger Baumgardt at the $<1\sigma$ level (i.e., $(\mu_\alpha \cos\delta, \mu_\delta)=(3.251 \pm 0.005; -17.649 \pm 0.005)$ mas yr^{-1}).

Appendix B: Artificial-star tests

We computed artificial-star tests to correct for systematic errors between input magnitude and recovered magnitudes and to estimate the level of completeness in our data. We setup our tests for each cluster as in, for example, Bellini et al. (2017a) and Nardiello et al. (2023a).

We generated a set of artificial stars with F150W magnitude from close to the saturation limit to $m_{\text{F150W}} \sim 33$, i.e., several magnitude below the faintest star in our sample. For the Southern field of NGC 6121, we simulated 100 000 stars with a colors that lie on a fiducial line representing the MS of the cluster, drew by hand in the observed CMDs with the other F606W and F814W filters. We also simulated 100 000 stars along the WD sequence and 50 000 stars with random colors to simulate the distribution of field objects. For the Northern field of NGC 6121, which overlap with existing HST data is smaller than that between HST and the Southern field, we reduced the numbers to 40 000 MS and WD stars and 20 000 field sources (i.e., about the same number of stars per arcmin^2). Finally, for NGC 6397, we instead created 200 000 stars along the MS, 100 000 WDs and 50 000 field objects. All fields analyzed in our work show a rather uniform distribution of objects, thus we assigned to all these stars random positions to uniformly cover the field of view.

We then used the KS2 software to add to each image one artificial star at a time, and then find and measure this source in the same way as done with the real data. Figure B.1 shows an example for NGC 6397. The CMD with the artificial stars given in input is shown in the middle panel, whereas the CMD made with the KS2-based output is shown in the rightmost panel. Both
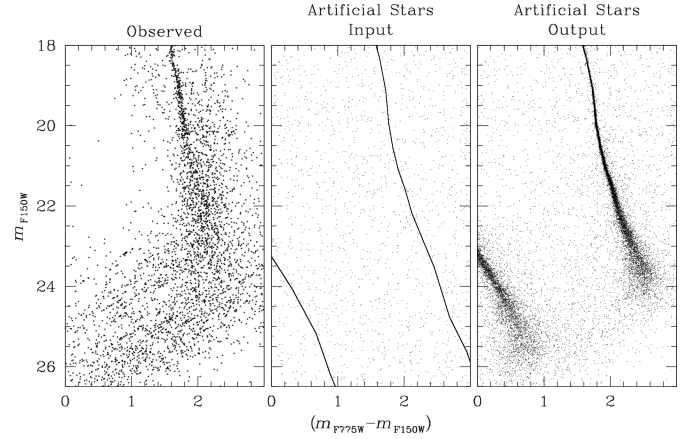

Fig. B.1. Example of artificial-star test for NGC 6397. (Left): lCMD of the stars measured in the field of NGC 6397. (Middle and Right): CMDs highlighting the artificial stars in input and output from our test, respectively. Only 10% of the points are shown, for the sake of clarity.

the observed and the output CMDs in this Figure are corrected for the so-called input-output systematic error (e.g., Bedin et al. 2019), which consists in an increasingly-larger overestimate of the flux of a star towards fainter magnitudes. We corrected the difference between the inserted and recovered values of magnitudes of the artificial stars following the prescriptions of Bedin et al. (2009). In our work, we find that such correction is small (<0.1 mag at most) in F150W and it increases for bluer filters, reaching even 0.3 mag for faint stars in the F606W filter. When the completeness drops below 50%, the input-output correction is less constrained, so for stars fainter than this threshold, the correction was kept fixed at the value of the last reliable estimate. This means that for stars with very low completeness, the correction could be underestimated. All CMDs presented in our work are corrected for this input-output effect.

The artificial-star tests also allow us to estimate the completeness level in our CMDs. The completeness is defined as the ratio between the number of recovered and injected stars. A star was considered as recovered if the output and input positions differ by less than 0.5 pixel, the difference between output and input magnitudes is less than 0.75 mag, and the star passed the quality selections described in Sect. 4. All these criteria have to be fulfilled in both the HST and JWST data. Figures C.1 and C.2 presents the results for NGC 6121 and NGC 6397, respectively. In both cases, we can see that the number of sources along the MS drops when the completeness is still high, meaning that the density of stars we see in that region of the CMD is real. For NGC 6121, the completeness is higher for the Southern field, where the depth of coverage of both the HST and JWST is more uniform. On the other hand, the low completeness along the WD sequence prevents us from studying in detail the WD cooling sequence. Finally, the large cell-to-cell variation in regions of the CMDs not covered by cluster stars, especially in the Northern field of NGC 6121, is due to the relatively-low number of field stars simulated in our test.

The main limitation in our work is the depth of the HST data. Indeed, if we compute the completeness level of the F150W NIRISS data alone, we find that the 50% level is at about $m_{\text{F150W}} = 25$ and 26.5 for NGC 6121 and NGC 6397, respectively. Additional deep observations are thus paramount to completely exploit these JWST data.

Appendix C: Electronic material

We make our astro-photometric catalogs and stacked images publicly available. We release one catalog for each cluster that contains: equatorial coordinates in ICRS at the epoch of the JWST observations; x and y JWST master-frame positions (in pixel; pixel scale of 40 mas pixel^{-1}); ID number of the source; photometric information for each filter; membership flag (flag=1 for cluster members and 0 otherwise). For NGC 6121, we also include a flag to discriminate between objects measured in the Northern (flag=1) and Southern (flag=2) fields.

For each filter, we provide: the calibrated VEGA magnitude corrected for differential reddening and for the input-output correction (Appendix B); the raw instrumental magnitude; saturation flag (flag=0 for unsaturated objects and 9 otherwise); magnitude rms; quality-of-PSF-fit (QFIT) parameter; fractional flux within the fitting radius prior to neighbor subtraction; number of exposures in which a source was found; number of exposures used to measure the flux of a source; RADXS value; sky value; and sky rms.

We emphasize the following:
– We included all objects detected in the JWST/NIRISS images and provide ancillary information from the HST data only for the sources found in common.
– We give a PM-based membership flag because improved PMs will be computed with state-of-the-art techniques (Bellini et al. 2014; Libralato et al. 2022) in a subsequent paper of the series.
– The 0.05-mag offset between the photometry in the Northern and Southern fields of NGC 6121 (Sect.3.1) is included in the calibrated magnitude but not in the instrumental ones.
– All photometric quantities for a source are set to 0 if it is not measured in a given filter/camera/epoch.
– All photometric quantities but the magnitudes are set to 0 if a source is saturated.
– As described in Appendix B, the input-output correction when the completeness level drops below ~50% is less constrained, so for stars fainter than this threshold, the correction was kept fixed at the value of the last reliable estimate. For NGC 6121, this threshold for each filter is: $m_{F150W}^{Northern} \sim 25.7$, $m_{F150W}^{Southern} \sim 24.7$, $m_{F606W} \sim 27.2$, $m_{F814W} \sim 25.2$. For NGC 6397, the threshold is set at $m_{F150W} \sim 26.3$, $m_{F775W} \sim 26.4$.
– The input-output correction for saturated stars included in the calibrated magnitudes is extrapolated from the unsaturated sources and it should not be considered in any analysis.
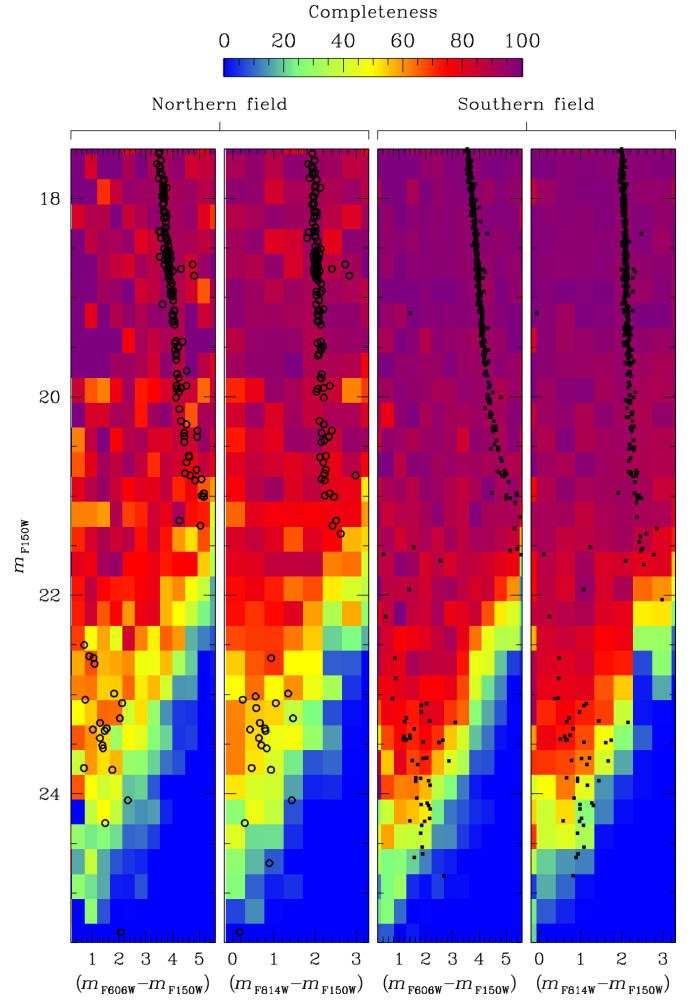

Fig. C.1. Completeness level for the Northern and Southern fields of NGC 6121. In each CMD, cells are color-coded according to the completeness level of stars in the corresponding magnitude-color interval (see the color bar at the top). Points, with the same symbols as in Fig. 2, are the observed cluster members in our data.
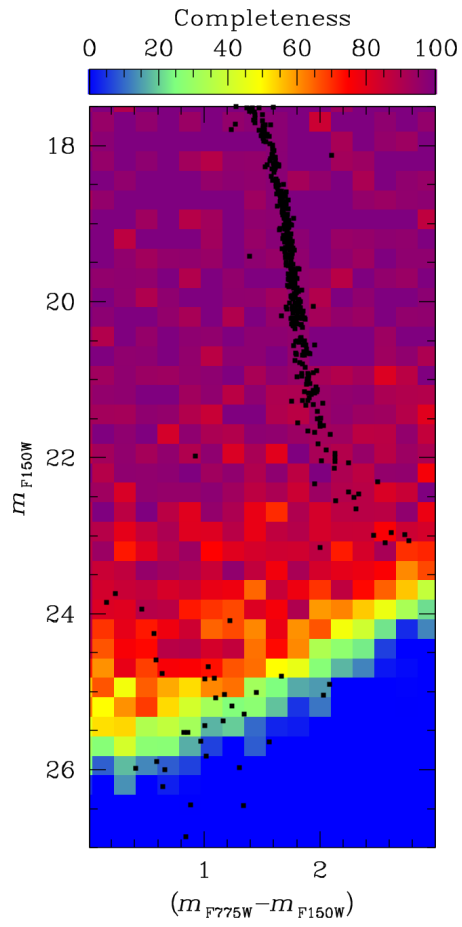
Fig. C.2. Same as Fig. C.1 but for NGC 6397.